

# Stabilisation of FeCoNiCuPt high-entropy alloy nanoparticles by surface capping

Anurag Sharma  and Andrew L. Hector  \*

Received 22nd May 2025, Accepted 29th July 2025

DOI: 10.1039/d5fd00088b

High-entropy alloys (HEA) are a distinct class of materials made up of multiple principal components ( $\geq 5$ ) in near-equimolar ratios, resulting in extraordinary properties, including high catalytic activity, corrosion and oxidation resistance, and tunable magnetic properties. In nanoparticle form, these alloys are highly promising for a variety of advanced applications, such as catalysis, magnetic storage, and biomedical technology [Zoubi *et al.*, *Nano Energy*, 2023, **110**, 108362]. This study used an isolating-medium-assisted solid-state reaction to synthesise FeCoNiCuPt HEA nanoparticles with ultrafine NaCl particles as the isolating medium [Meng *et al.*, *Mater. Adv.*, 2024, **5**, 719]. The nanoparticles were stabilised with a range of hydrophobic and hydrophilic capping agents, such as polyethylenimine, polyvinylpyrrolidone, stearic acid, octadecylamine, etc., introduced before or after the removal of the isolating medium. The formation of single-phase nanoparticles and the chemical composition of FeCoNiCuPt was validated using X-ray diffraction and energy-dispersive X-ray spectroscopy. Transmission electron microscopy and dynamic light scattering were used to determine particle sizes, effective capping agent thickness, and particle stability. The results highlight the successful synthesis of the FeCoNiCuPt nanoparticles, the effect of capping agents on the control of particle size, and the stability of capped-nanoparticle suspensions in water and organic solvents. The study emphasises the importance of selecting the appropriate capping agent to maintain nanoparticle stability and prevent agglomeration.

## 1 Introduction

High-entropy alloys (HEAs) are made up of several elements ( $\geq 5$ ) in about an equimolar ratio (with 5% to 35% variability).<sup>1</sup> Yeh describes a “high-entropy alloy” as an alloy material with the maximum mixing entropy, resulting in solid solution phases, unlike other non-equiautomic compositions.<sup>1,2</sup> HEAs with transition metals like Fe, Co, and Ni have attracted special attention because of their optical, photonic, catalytic, and magnetic properties. Bazioti *et al.* investigated a series of materials based on  $\text{FeCoNiAlMn}_x$  and found strong ferromagnetism with low coercivity values ( $<1000 \text{ Am}^{-1}$ ).<sup>3</sup> The FeCoNiTiAl HEA synthesised by Liu *et al.*

School of Chemistry and Chemical Engineering, University of Southampton, Highfield, Southampton, UK.  
E-mail: a.l.hector@soton.ac.uk



demonstrated good nonlinear optical features at 1030 and 1560 nm and has significant potential for progress in the pulsed laser field in harsh environments.<sup>4</sup> The FeCoNi-based HEA developed by Liao *et al.* can absorb light across the spectrum (250–2500 nm), demonstrating 99% photothermal conversion efficiency under 1 solar irradiation.<sup>5</sup> FeCoNiCuPt performs exceptionally well in the methanol oxidation and hydrogen evolution reactions and shows 2.70 times more electrochemically active surface area compared to a commercial Pt/C catalyst.<sup>2</sup> The FeCoNiCuIr HEA also performs well in the oxygen evolution process, attaining a low overpotential of 360 mV at 10 mA cm<sup>-2</sup> and retaining >94% of the current after 10 hours.<sup>6</sup> These examples demonstrate the remarkable magnetic, optical and catalytic capabilities of FeCoNi-based HEAs.

HEAs perform noticeably better when synthesised as nanoparticles. Compared to their bulk counterparts, their physical and chemical properties change dramatically as the surface-to-volume ratio, structural disorder, and quantum confinement effect increase. When Pan *et al.* loaded FeCoNiMnCr nanoparticles into N-doped carbon nanotubes, zinc-air batteries demonstrated improved stability (200 hours) and power density (214 mW cm<sup>-2</sup>) compared to bulk FeCoNiMnCr because of their larger surface area and constituent element interaction.<sup>7</sup> FeCoNiMnCr nanoparticles outperformed bulk FeCoNiMnCr in bifunctional oxygen reaction activity applications because they offer more active sites and tunable surface chemistry.<sup>7</sup> Das *et al.* synthesised NbCrTaVW HEA nanoparticles and bulk samples and discovered that when the bulk alloy was milled to ~12 nm crystallite size, it changed from being diamagnetic to superparamagnetic,<sup>8</sup> showing small coercivity (~0) and saturation magnetisation approaching ~7 emu g<sup>-1</sup>. Larger bulk domains fragmented and acted as superparamagnetic spins as the particle size reduced to nanoscale.<sup>8</sup> Overall, FeCoNi-based HEA nanoparticles are a promising research field and an important material class for future functional nanomaterials.

Smaller nanoparticles exhibit novel quantum size effects<sup>9</sup> and change the electronic structure of HEA materials, but their greater surface energy causes Ostwald ripening, aggregation, and surface energy reduction. Uncontrolled nanoparticle aggregation harms its applications and must be prevented.<sup>10</sup> Even though HEA nanoparticles have tremendous potential, stabilising colloids and preserving small particle size during processing after synthesis and storage is challenging. In particular, HEA nanoparticles made *via* solid-state techniques tend to settle or aggregate together over time, especially when dissolved in solvents like ethanol.<sup>10</sup> Das *et al.* also found that nanoparticle suspension stability depends on solvent choice. In ethanol and acetone, nanoparticles were seen to grow and aggregate instantly.<sup>11</sup> Thus, nanoparticle stability, dispersibility, and physical property tunability necessitate efficient surface capping.

Surfactants, ligands, and polymers have been utilised to cap nanoparticles to control Ostwald ripening, particle size, shape, and stability.<sup>12</sup> These compounds inhibit nanoparticle growth and aggregation by binding to, and lowering, surface energy.<sup>13</sup> Thiols, amines, and surfactants like oleylamine, oleic acid, and PEG derivatives are common capping materials applied on nanoparticles. Dey *et al.* applied oleylamine as a capping agent and solvent on HEA nanoparticles with varied combinations of Pd, Pt, Rh, Ir, Ni, Fe, Co, and Sn and obtained particles with <15 nm diameters.<sup>14</sup> Da Silva *et al.* reported the synthesis of FeCoNiRuPt HEA nanoparticles using oleylamine and oleic acid as surfactants, which restricted



Ostwald ripening and particle growth, keeping the average particle size to  $<5$  nm.<sup>15</sup> Sun *et al.* produced AuAgCuPtPd HEA nanoparticles, which ranged in diameter from 0.5 to 3 nm and were capped using thiolated polymer ligands.<sup>16</sup> In this work, copper and platinum were chosen as the constituent elements to incorporate in FeCoNi-based, 5-element FeCoNiCuPt HEA nanoparticles. Copper, like zinc or other antioxidant metals, tends to stabilise the alloy by reducing the rate at which the nanoparticles oxidise or dissolve, thus increasing the durability of the HEA nanoparticles.<sup>17</sup> Pt and FePt are well-known for their high-performance electrocatalytic properties.<sup>18</sup> FePt alloys have significantly high magnetic anisotropy too.<sup>19</sup> Combining Cu and Pt with the well-studied FeCoNi group can enhance the durability, catalytic activity, and magnetic properties in HEAs by creating multi-element “cocktail” effects.<sup>17–19</sup>

Solid-state reaction as a synthesis method yields a clean, organic surfactant (ligand)-free surface of the product. In the literature, the isolating medium—which often uses NaCl, KCl, or MgO—has been frequently employed to produce FePt, FeCuPt, and other multi-metallic Pt alloys.<sup>1,19,20</sup> These isolating mediums behave as a substrate (separating matrix) and ensure heat is applied evenly and the particles stay separated, preventing nucleated particles from aggregating, and preventing nanoparticle sintering as the annealing process progresses, leading to a small particle, single-phase alloy with high thermal stability.<sup>1,21</sup> That is why the isolating medium-assisted solid-state reaction method was chosen to synthesise the FeCoNiCuPt HEA nanoparticles and study the effect of different capping agents on the particle size growth of capped FeCoNiCuPt HEA nanoparticles and their suspension stability. Meng and their group had synthesised the ultra-small (3–7 nm) FeCoNiCuPt HEA nanoparticles using the same synthesis method to investigate their electrocatalytic properties.<sup>2</sup>

*In situ* (during NaCl dissolution) and post-synthesis (after washing away NaCl and suspending in ethanol) capping treatments were performed on nanoparticles to determine the best method for applying capping agents to maintain dispersion and suspension stability and to control Ostwald ripening and particle growth. The thirteen capping agents evaluated included polymers like Pluronic P123 and polyvinylpyrrolidone, surfactants like sodium dodecyl sulfate (SDS) and hexadecyltrimethylammonium bromide (CTAB), amines like hexadecylamine, oleylamine, octylamine, and octadecylamine, organic acids like citric, oleic, and stearic acid, and other common stabilizers like octadecene and polyethylenimine-linear. The capped and uncapped HEA nanoparticles were characterised using X-ray diffraction (XRD), energy-dispersive X-ray spectroscopy (EDS), transmission electron microscopy (TEM), and dynamic light scattering (DLS) to evaluate their crystallographic structure, elemental composition, particle size distribution of the metal core and capping layer of nanoparticles, and stability of suspension. The objective was to identify capping agents that resulted in small particle sizes, minimal aggregation and good stability of the FeCoNiCuPt nanoparticle suspension.

## 2 Experimental

### 2.1 General procedure for the synthesis of FeCoNiCuPt HEA nanoparticles

For the synthesis of 1 mmol (432.1 mg) FeCoNiCuPt nanoparticles, the previously reported isolating medium-based solid-state reaction method was used,<sup>2</sup> where



1 mmol of precursors  $\text{Fe}(\text{C}_5\text{H}_7\text{O}_2)_3$  (0.3528 g),  $\text{Co}(\text{C}_5\text{H}_7\text{O}_2)_3$  (0.356 g),  $\text{Ni}(\text{C}_5\text{H}_7\text{O}_2)_2$  (0.2568 g),  $\text{Cu}(\text{CH}_3\text{COO})_2$  (0.1816 g), and  $\text{Pt}(\text{C}_5\text{H}_7\text{O}_2)_2$  (0.3936 g) were added together in 1400 mL of a 1:1 hexane/ethanol mixture to prepare a precursor solution at 50 °C while stirring continuously till complete dissolution of the precursors. Ultrafine NaCl powder (grain size <10 µm) purchased from Sun Science Ltd (300 times the total precursor weight, ~463.78 g) was mixed into the precursor solution and this was heated and stirred at 80 °C until the solvent had all evaporated. The resultant powder was transferred to a Lenton split tube furnace (model no. CSC 12, max. temperature 1200 °C) in a quartz boat and heated under a 5% hydrogen and 95% argon environment at 10 °C minute<sup>-1</sup> to 600 °C, where it stayed for 3 hours before cooling to room temperature. Since some powder adhered to the quartz boat, the product weighed 457.3 g. Fourteen batches of 13.72 g of sintered powder were dissolved separately in 90 mL of DI water. The mixture was put in three 50 mL capacity centrifuge tubes, 30 mL each, and centrifuged (4500 rpm, 30 minutes) three times with 30 mL of DI water added after the previous suspension was decanted and once with 30 mL of ethanol added, using a Heraeus Megafuge 8 centrifugation machine. Each batch of nanoparticles was collected together and stored by suspending them in 50 mL of ethanol at -20 °C for post-synthesis capping and characterisation. Sintered powder for *in situ* capping was stored separately.

## 2.2 Procedure for capping of FeCoNiCuPt nanoparticles

Thirteen capping agents were applied to FeCoNiCuPt nanoparticles by two distinct methods. In “post-synthesis” capping, the capping agents were added after the nanoparticles had been purified, washed, and stored in ethanol. In “*in situ*” capping, the capping agents were incorporated during the washing of the annealed powder while the sodium chloride was being removed.

**2.2.1 Post-synthesis capping of FeCoNiCuPt nanoparticles.** 0.3 mmol of each hydrophilic capping agent—Pluronic P123 (1.74 g), polyvinylpyrrolidone (3 g), SDS (0.0865 g), CTAB (0.1093 g), polyethylenimine-linear (1.5 g), and citric acid (0.0576 g)—were dissolved in 90 mL of water separately, forming 3.33 mM solutions. Six batches of nanoparticles suspended in ethanol were centrifuged for 30 minutes, and the ethanol was decanted. The nanoparticles were suspended in the capping agent solutions, ultrasonicated for 5 minutes and stirred for 1 hour. Similar centrifuge steps were followed for these mixtures, where nanoparticles were washed and centrifuged (4500 rpm, 30 minutes) three times with 30 mL of DI water and once with 30 mL of ethanol. The resultant capped materials were collected and suspended in 50 mL of DI water.

For the hydrophobic capping agents, 0.3 mmol of the solid or liquid capping agent—hexadecylamine (0.068 g), stearic acid (0.0853 g), octadecylamine (0.0848 g), oleic acid (density: 0.895 g cm<sup>-3</sup>, 0.0946 mL), oleylamine (density: 0.813 g cm<sup>-3</sup>, 0.0987 mL), octadecene (density: 0.789 g cm<sup>-3</sup>, 0.096 mL), and octylamine (density: 0.782 g cm<sup>-3</sup>, 0.0497 mL)—were dissolved separately in 90 mL of toluene at room temperature, forming a 3.33 mM solution. Seven batches of stored nanoparticle suspensions were centrifuged for 30 minutes and the ethanol decanted before mixing in the capping agent solution. The mixture was ultrasonicated for 5 minutes and stirred for 1 hour. These 90 mL mixtures were centrifuged (4500 rpm, 30 minutes) in three centrifuge tubes in equal



amounts, with 30 mL of toluene added in each bottle after the previous suspension was decanted. This centrifuging process was repeated thrice. The capped nanoparticles were collected and suspended in 50 mL of toluene.

**2.2.2 *In situ* capping of FeCoNiCuPt nanoparticles.** The hydrophilic agents Pluronic P123 (1.74 g), polyvinyl pyrrolidone (3 g), SDS (0.0865 g), CTAB (0.1093 g), polyethylenimine-linear (1.5 g), and citric acid (0.0576 g)—were combined with 90 mL of water until complete dissolution resulted in 3.33 mM solutions. Later, 13.72 g of sintered powder was added to each solution and stirred for 1 hour. Similar centrifuge methods were used for these solutions, with the nanoparticles cleaned, centrifuged and washed (4500 rpm, 30 minutes) three times with 30 mL of DI water and once with 30 mL of ethanol. The resulting capped materials were collected and suspended in 50 mL of DI water.

0.3 mmol of each hydrophobic capping agent—hexadecylamine (0.068 g), stearic acid (0.0853 g), octadecylamine (0.0848 g), oleic acid (0.0946 mL), oleylamine (0.0987 mL), octadecene (0.096 mL), and octylamine (0.0497 mL)—was dissolved in 90 mL of toluene at room temperature, forming a 3.33 mM solution. After adding 13.72 g of sintered powder, the solutions were stirred for 1 hour. These solutions were mixed with 90 mL of DI water in a separating funnel by shaking the funnel for 15 minutes, to dissolve the NaCl. The funnel was rested horizontally until both liquids separated. Water was separated out of the mixture. The remaining mixture inside the separating funnel was centrifuged three times (4500 rpm, 30 minutes) in three centrifuge tubes, with 30 mL of toluene added to each bottle after decanting the preceding supernatant, and the capped materials were collected and suspended in 50 mL of toluene.

### 2.3 X-ray diffraction (XRD)

The phase purity and structural parameters of FeCoNiCuPt were determined using a Rigaku SmartLab diffractometer employing a copper source of  $K\alpha$  radiation with  $\lambda = 1.5406 \text{ \AA}$  at ambient temperature.<sup>22</sup> An XRD scan was taken in the  $35\text{--}100^\circ 2\theta$  range, with  $0.01^\circ$  step size in Bragg–Brentano geometry. Rietveld refinement of the XRD pattern using GSAS II was applied to extract the lattice parameters. The background was fitted using the Chebyshev function, and the instrumental peak shape was defined from a standard LaB<sub>6</sub> sample. The Rietveld-refined XRD pattern of FeCoNiCuPt was plotted using OriginPro software.

### 2.4 Energy-dispersive X-ray spectroscopy (EDS)

A Zeiss Sigma 500 VP FESEM with an Oxford Instruments Ultim 170 EDS detector was used to determine the material's elemental composition. The ethanol dispersion was centrifuged (4500 rpm, 30 minutes) to extract the uncapped nanoparticles, then left to evaporate any remaining ethanol for an hour. For EDS measurement, the powder was placed on a stub covered with carbon tape.

### 2.5 Transmission electron microscopy (TEM)

The morphology and particle size distribution of all the capped and uncapped FeCoNiCuPt nanoparticles were examined using an FEI Tecnai T12 transmission electron microscope fitted with a Morada G2 digital camera (11 MP) at  $120\times$  kV maximum accelerating voltage and  $400\,000\times$  maximum magnification. The suspended particles were ultrasonicated for 5 minutes, drop-cast on the carbon grids

and left to dry for one hour to get rid of the residual solvent prior to TEM analysis. To estimate the particle size distribution and average diameter, 200 spherical nanoparticle diameters were manually measured from TEM micrographs using ImageJ software.<sup>23,24</sup> The kernel density distribution function was used to measure particle frequency throughout a size range.<sup>25</sup>

## 2.6 Dynamic light scattering (DLS)

Anton Paar's Litesizer DLS 701 instrument was used to examine the particle size distribution and for zeta potential measurement of the capped nanoparticles. The instrument was equipped with laser light of wavelength 658 nm from a single-frequency laser diode, providing 40 mW, with a particle diameter measurement range of 0.3 nm–10  $\mu$ m and a zeta potential measurement range of  $>\pm 1000$  mV. The suspended capped nanoparticles were ultrasonicated for 5 minutes and filtered with a 100 nm syringe filter to remove any agglomerates. The particle size distribution of particles suspended in water and toluene was measured using disposable and quartz cuvettes, respectively. Omega cuvettes and univettes were used to measure the nanoparticle zeta potential in water and toluene.

## 3 Results and discussion

The XRD pattern of the uncapped FeCoNiCuPt HEA alloy was Rietveld-refined, with a 1.694 goodness of fit ( $\chi^2$ ) and a 2.307% weighted profile *R*-factor ( $R_w$ ) showing a strong alignment between the calculated pattern and the observed profile. The Rietveld-refined XRD pattern of the single-phase FeCoNiCuPt HEA nanoparticles is displayed in Fig. 1.

The diffraction pattern of the synthesised FeCoNiCuPt material (uncapped) can be indexed using the database of individual elements, Fe (PDF code: 9014285), Co (PDF code: 9011619), Ni (PDF code: 2100640), Cu (PDF code: 4105681), and Pt (PDF code: 1011103), as shown in Fig. 1. The diffraction peaks at

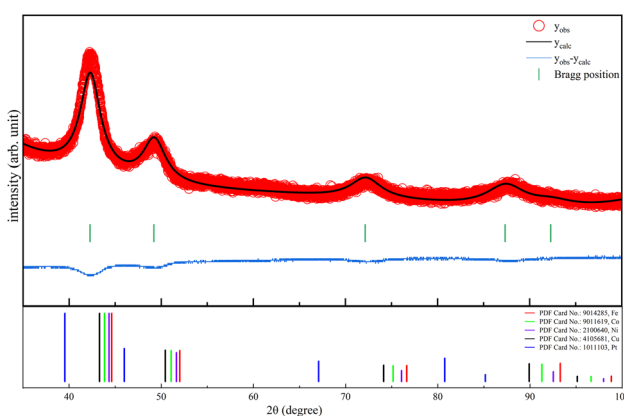


Fig. 1 The Rietveld-refined XRD patterns of the uncapped FeCoNiCuPt sample and corresponding PDF standard patterns of constituent elements of the  $Fm\bar{3}m$  (225) space group. Red circles, black line, blue line and green vertical signs represent the observed ( $Y_{\text{obs}}$ ), calculated ( $Y_{\text{calc}}$ ), the difference between the observed and calculated spectra ( $Y_{\text{obs}} - Y_{\text{calc}}$ ), and Bragg positions, respectively.



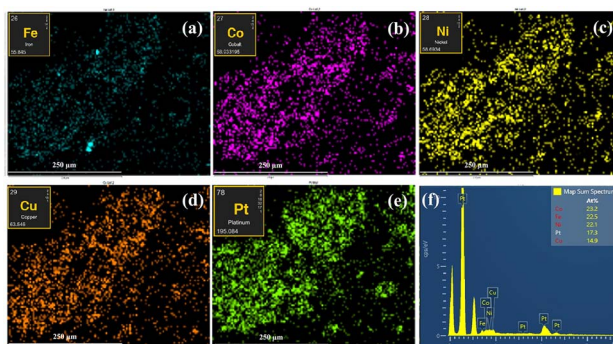


Fig. 2 (a–e) Elemental mapping images of uncapped FeCoNiCuPt HEA particles, and (f) their EDS spectra.

42.27°, 49.21°, 72.15°, 87.33°, and 92.30° 2θ values can be indexed to the 111, 200, 220, 311 and 222 reflections of cubic  $Fm\bar{3}m$  (225) space group material, with lattice parameter  $a = 3.699(8)$  Å, consistent with the previously reported values.<sup>2</sup> The atomic radius of platinum is comparatively larger (~139 pm) than that of the other elements (~124–128 pm) in the alloy. When FeCoNiCuPt is produced, its average lattice spacing becomes intermediate between the constituent element lattice spacings, producing HEA XRD peaks that show up in between the pure element peaks,<sup>2</sup> as seen in Fig. 1.

The elemental distributions of the uncapped FeCoNiCuPt HEA are shown in Fig. 2(a–e). The elements Fe, Co, Ni, Cu, and Pt are uniformly distributed together, indicating their alloying in the HEA nanoparticles. Fig. 2(f) represents the EDS spectra showing the atomic weight of constituent elements, % of Fe, Co, Ni, Cu, and Pt as 22.5%, 23.2%, 22.1%, 14.9% and 17.3%, respectively, which are close to the equal proportions range stated by Yeh *et al.*, proving the synthesis of the FeCoNiCuPt HEA.<sup>1</sup> Meng *et al.* suggest that the copper precursor ( $Cu(CH_3COO)_2$ ) reacts with NaCl during annealing at high temperature (600 °C), resulting in the formation of water-soluble salts like  $CuCl_2$  that dissolve during the washing process to collect HEA nanoparticles, resulting in reduced Cu content.<sup>2,26</sup>

The EDS spectra in Fig. 2(f) show carbon and oxygen  $K\alpha$  peaks at 0.277 keV and 0.525 keV, respectively.<sup>27</sup> The carbon peak in the EDS spectra comes from mounting the sample on carbon tape (Fig. S1(b)), as well as due to the presence of adventitious carbon because of the deposition of carbonaceous materials on the sample when they are exposed to the environment.<sup>28</sup> The presence of oxygen, as shown in Fig. S1(c), may be due to surface particle oxidation while washing because FeCoNi-based HEAs are vulnerable to oxidation in air and water, though previous research shows a much lower rate of oxidation of FeCoNiCuPt HEA nanoparticles than their monometallic counterparts.<sup>29</sup>

### 3.1 TEM analysis of uncapped FeCoNiCuPt nanoparticles

The TEM micrographs of uncapped FeCoNiCuPt HEA nanoparticles are presented in Fig. 3, where Fig. 3(a) shows the TEM micrograph of particles analysed after 1 hour of washing out the isolating medium and Fig. 3(b) shows particles analysed



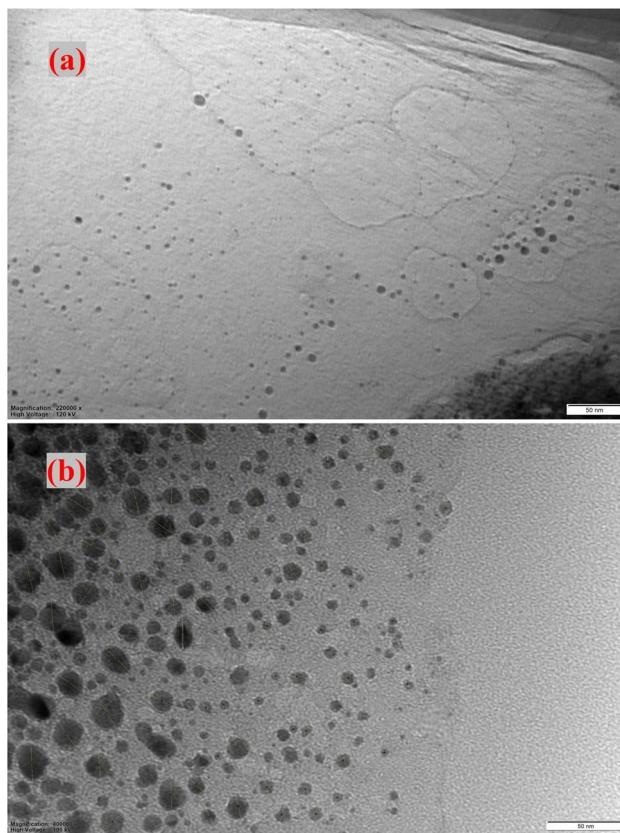


**Fig. 3** TEM image micrographs of uncapped FeCoNiCuPt nanoparticles taken (a) after 1 hour and (b) after 10 days of washing out the isolating medium and storing in ethanol at  $-20\text{ }^{\circ}\text{C}$ .

after 10 days of washing, which were stored in ethanol at  $-20\text{ }^{\circ}\text{C}$ . The TEM particle size distributions were computed using about 200 particles in the field of view of a single TEM micrograph. Although the distributions are based on individual micrographs, examining a large number of particles increases their statistical significance and provides a good estimate of particle size distribution.

Most nanoparticles are spherical, with darker black circles suggesting thicker and overlapped particles, and lighter black circles showing individual nanoparticles. This difference in appearance is explained by the electron beam's higher scattering in areas with overlapping particles or thicker samples. Electrons interact with more material as they move through thicker regions of the sample, which causes more scattering and a lower transmitted beam intensity.<sup>30</sup>

Within 10 days of storage in ethanol, the average particle size of uncapped nanoparticles increased by 165% from 4.7 nm to 12.6 nm. Fig. 3(b) reveals agglomeration of two or more particles in uncapped FeCoNiCuPt nanoparticles after 10 days, resulting in darker and larger spheres. The minimum and maximum particle sizes observed for the sample analysed after 1 hour of washing are 1.4 nm and 13.9 nm, respectively, compared to 2.3 nm and 33.1 nm,



respectively, for particles held for 10 days. The  $D_{10}$ ,  $D_{50}$  and  $D_{90}$  values representing the smallest 10%, 50% and 90% of the particles by size, respectively, had average particle sizes of 2.0 nm, 3.3 nm, and 4.3 nm, respectively, increasing to 2.8 nm, 6.2 nm, and 10.8 nm for the sample stored in ethanol for 10 days. Fig. 4(a) displays the particle size distribution for both samples, indicating a decrease in the number of smaller nanoparticles and a shift in the size distribution to larger uncapped FeCoNiCuPt nanoparticles over time. It is clear that particle size and agglomeration increase over time, even when suspensions are stored in ethanol at a low temperature. Due to the increase in specific surface area with the decrease in particle size, nanoparticles contain a huge amount of surface energy, which challenges the system's thermodynamic behaviour to reach a minimum energy, resulting in the Ostwald ripening and agglomeration of nanoparticles.<sup>31,32</sup> A large amount of repulsive force is required to defeat the thermodynamic interactions

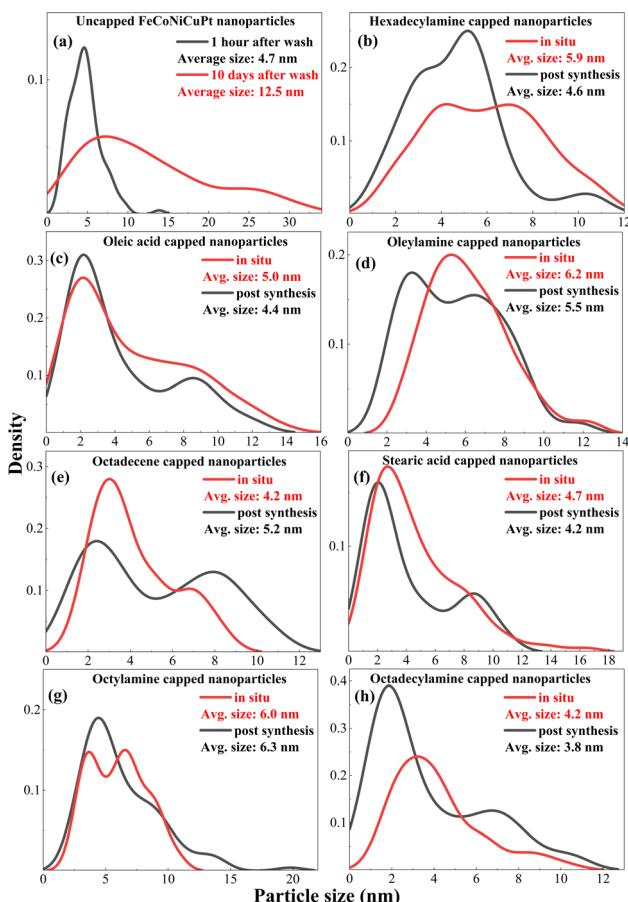


**Fig. 4** Particle size distribution plots of nanoparticles from analysis of TEM micrographs for (a) uncapped FeCoNiCuPt nanoparticles analysed after 1 hour (black) and 10 days (red), and nanoparticles capped by hydrophobic capping agents (b) hexadecylamine, (c) oleic acid, (d) oleylamine, (e) octadecene, (f) stearic acid, (g) octylamine, and (h) octadecylamine, where the red and black lines represent the *in situ* capped and post-synthesis capped nanoparticles, respectively.



between nanoparticles, and that is why the need for capping agents arises.<sup>32,33</sup> To prevent nanoparticle agglomeration and stabilise the suspension, 13 capping agents were employed, including polymers, surfactants, amines, acids, *etc.* These capping agents were separated into two groups according to their hydrophilic or hydrophobic nature.

### 3.2 TEM analysis of hydrophobic-agent-capped FeCoNiCuPt nanoparticles

The particle size distribution plots of nanoparticles with hydrophobic capping agents are given in Fig. 4(b)–(h), with red and black lines indicating *in situ* and post-synthesis capping, respectively. Fig. S2 and S3 show their TEM micrographs. The particle size distributions were plotted using the kernel smooth distribution function, as this estimate is nonparametric and can be used in almost any situation, regardless of particle size or aggregation.<sup>25</sup> Octadecylamine-capped nanoparticles, both *in situ* and post-synthesis, exhibited the lowest average particle sizes among the seven hydrophobic capping agents. Post-synthesis octadecylamine-capped nanoparticles have an average particle size of 3.8 nm, nearly 10% smaller than *in situ*-capped nanoparticles (4.2 nm). The minimum and maximum particle sizes for octadecylamine-capped nanoparticles post-synthesis are 1.0 and 10.7 nm, whereas *in situ* caps vary from 1.3 to 11.6 nm. This result indicates that octadecylamine is an effective hydrophobic capping agent under both capping conditions, helping to limit the increase in particle size.

Post-synthesis octadecylamine-capped nanoparticles have an ~20% lower particle size than uncapped FeCoNiCuPt nanoparticles (4.7 nm) observed one hour after washing. Similar trends are seen for the minimum and maximum particle sizes of octadecylamine-capped nanoparticles in comparison to uncapped nanoparticles, showing that nanoparticles start agglomerating just after washing away the NaCl.<sup>34,35</sup>  $D_{90}$  values for octadecene and oleic acid are  $<5$  nm, while for octadecylamine and stearic acid the  $D_{90}$  values are  $<4$  nm, as shown in Fig. 4, which are significantly lower than the particle size of uncapped nanoparticles. So, octadecylamine and stearic acid performed most effectively in retaining smaller particles among the examined hydrophobic agents.

### 3.3 TEM analysis of hydrophilic-agent-capped FeCoNiCuPt nanoparticles

Fig. 5 (a)–(f) shows particle size distribution graphs of all hydrophilic capping agents, with red and black lines representing *in situ* and post-synthesis capping agent introduction, respectively. Their TEM micrographs are shown in Fig. S4 and S5. Pluronic P123-capped nanoparticles exhibited the smallest average particle size among the six hydrophilic agents, with average particle sizes of capping *in situ* and post-synthesis being 3.8 nm and 3.3 nm, respectively. Post-synthesis Pluronic P123-capped nanoparticles range from 1.1 to 12.5 nm, whereas *in situ* octadecylamine-capped nanoparticles range from 1.2 to 14.8 nm. The average particle size of all hydrophilic-agent-capped nanoparticles is  $<5$  nm (SDS has an ~5 nm average particle size), whether applied *in situ* or post-synthesis.

The examination of 26 capped samples using 13 capping agents in two techniques found that 22 samples preserved  $D_{90}$  values below 5 nm, of which 15 samples had  $D_{90} < 4$  nm, highlighting the importance of capping agents in controlling nanoparticle size dispersion. Out of the thirteen capping agents



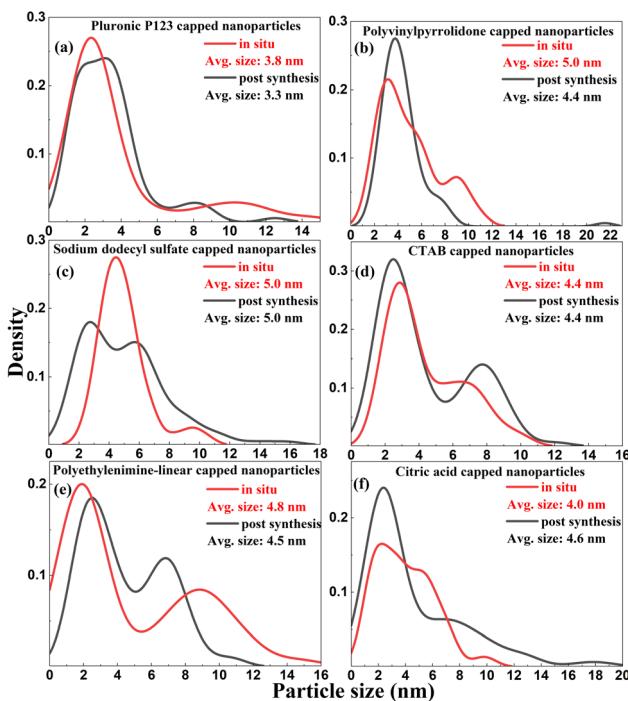


Fig. 5 TEM micrograph particle size distribution plots for hydrophilic-agent-capped nanoparticles (a) Pluronic P123, (b) polyvinylpyrrolidone, (c) SDS, (d) CTAB, (e) polyethylenimine (linear), and (f) citric acid, where red and black lines represent *in situ* and post-synthesis capped nanoparticles, respectively.

tested, the size dispersion of most of the nanoparticles was smaller when capping was done post-synthesis than *in situ*. This difference in size may be caused by the elimination of weakly bound nanoparticles, unreacted precursors, undissolved isolating medium, or excess capping agents through a series of washing operations.<sup>21,36</sup> It is important to make sure that the NaCl particles have completely dissolved and been eliminated by water centrifugation and ultrasonication before adding capping agents to the nanoparticles following sintering. This method ensures that the isolating medium is fully dissolved and that the capping agents only interact with the dispersed, pure nanoparticles. When employing hydrophilic capping agents, the size of the nanoparticles is mostly determined by the properties of the capping agent since the sintered powder was rinsed completely with water, dissolving the NaCl. As a result, the size of the hydrophilic-agent-capped nanoparticles is not significantly affected by whether they are added *in situ* or post-synthesis. In contrast, if hydrophobic capping agents are added *in situ* while the sintered powder still contains NaCl, they will coat both the nanoparticles and the NaCl matrix, as the hydrophobic capping agents are dissolved in toluene, and toluene is unable to dissolve NaCl. So the toluene suspension has the potential to interfere with NaCl dissolution, leaving residual salt in the end-product. This is demonstrated by the TEM micrographs of oleylamine and hexadecylamine (both hydrophobic) displayed in Fig. 6(a) and (b), respectively, in which undissolved NaCl particles can be observed. The post-washing capping



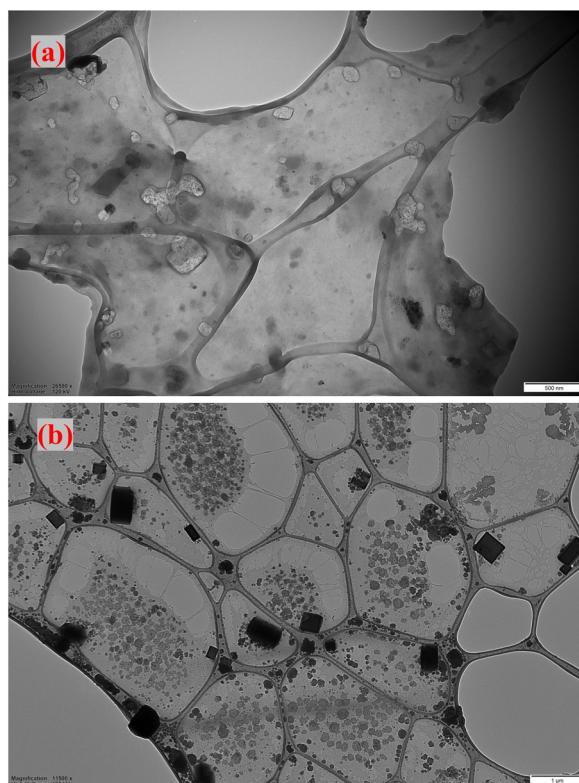


Fig. 6 TEM micrographs of FeCoNiCuPt HEA nanoparticles showing residual NaCl particles when capped with (a) oleylamine and (b) hexadecylamine introduced prior to washing (*in situ* capping) out the NaCl particles.

method is therefore advantageous for hydrophobic capping agents since it guarantees the elimination of NaCl, cleaner surfaces, and enhanced capping agent–nanoparticle contact, all of which reduce the risk of nanoparticle aggregation.

TEM analysis allowed us to analyse the particle size of individual nanoparticles; however, capped particles consist of a metal core, surface coating, and solvent molecules that are tightly associated with the coating. As a result, a capped nanoparticle's entire hydrodynamic diameter may be significantly larger than the individual particle size determined by TEM.<sup>37</sup> DLS analysis involves studying thousands of particles suspended in a solvent to provide a detailed hydrodynamic particle size distribution. The sizes of the particles are determined by examining the Brownian motion of the nanoparticles, which occurs due to their random movement as a result of collisions with solvent molecules. A laser is directed at the dispersed nanoparticles to facilitate this measurement. The hydrodynamic diameter ( $D_H$ ) of the capped nanoparticles was measured by employing the Stokes–Einstein equation within the instrument, which is affected by temperature and the dynamic viscosity of the solvent,<sup>38</sup> as shown in eqn (1):

$$D_H = \frac{k_B T}{3\pi\eta D}, \quad (1)$$



where  $k_B$  represents the Boltzmann constant,  $T$  represents temperature, and  $\eta$  is the viscosity of the solvent.

The particles were weighted by numbers in place of intensity or volume; the size of the most frequent particle in the solutions can be found by number-weighted particle size distribution. Agglomeration can result in the grouping of nanoparticles, which leads to their identification as larger particle clusters. The combined hydrodynamic size of these clusters is substantially greater than the size of individual particles, as measured by DLS. Moreover, the presence of even a few large particles and grouped clusters can result in a significant shift towards higher values in the resultant hydrodynamic diameter, particularly when measurements are conducted in intensity- or volume-weighted modes.<sup>39</sup>

### 3.4 DLS analysis of hydrophilic-agent-capped FeCoNiCuPt nanoparticles

Table 1 summarises the number-weighted particle size distribution of capped FeCoNiCuPt nanoparticles obtained using DLS. The most frequent particle size is denoted by  $D_M$ , while the smallest 10%, 50%, and 90% of particles are denoted by  $D_{10}$ ,  $D_{50}$ , and  $D_{90}$ , respectively.

The most frequent particle size ( $D_M$ ) of all these hydrophilic-agent-capped nanoparticles lies in the range of 10–80 nm, including both the metal core and the capping layer. As depicted in Table 1, Pluronic P123 gives the smallest hydrodynamic diameter with the most frequent particle size ( $D_M$ ) of 10.6 nm, which is consistent with the smallest metal core sizes found in TEM results. On the other hand, when post-synthesis capping is performed, CTAB, citric acid, and polyethylenimine have  $D_M \geq 70$  nm. Although the particle size of CTAB-capped nanoparticles is relatively larger than that of other nanoparticles, the particles

**Table 1** The experimentally observed particle sizes and zeta potential (ZP) of capped FeCoNiCuPt nanoparticles;  $D_{10}$ ,  $D_{50}$ , and  $D_{90}$  represent the average particle size of the smallest 10%, 50%, and 90% of particles, respectively, and  $D_M$  represents the most frequent particle size

Capping agent	Post-synthesis					<i>In situ</i>				
	$D_{10}$ (nm)	$D_{50}$ (nm)	$D_{90}$ (nm)	$D_M$ (nm)	ZP (mV)	$D_{10}$ (nm)	$D_{50}$ (nm)	$D_{90}$ (nm)	$D_M$ (nm)	ZP (mV)
Pluronic P123	11.4	48.4	53.1	50.6	−23.2	3.1	9.9	11.9	10.6	−17.1
Polyvinylpyrrolidone	23.4	39.9	55.0	44.5	−18.3	26.4	47.6	71.7	53.5	−25.6
Sodium dodecyl sulfate	15.4	41.6	43.5	43.0	−16.2	17.7	35.8	46.7	39.1	−12.9
CTAB	71.9	77.2	82.6	80.2	22.3	30.0	43.3	58.5	47.6	25.3
Polyethylenimine-linear	41.9	65.8	94.0	74.5	32.9	15.1	29.9	37.8	33.0	32.0
Citric acid	35.0	64.9	92.0	73.5	−24.4	4.6	22.1	39.6	43.9	−26.8
Hexadecyl amine	22.2	26.6	34.0	28.8	9.8	6.4	19.4	25.2	21.3	16.6
Oleic acid	3.7	11.8	15.2	12.9	13.8	8.8	24.4	28.5	25.8	15.9
Oleylamine	4.2	15.9	19.4	17.1	33.3	48.5	56.6	73.4	61.0	24.2
Octadecene	2.5	5.4	6.8	5.9	17.9	8.1	19.2	28.6	22.0	19.1
Stearic acid	15.5	51.0	68.3	56.6	24.2	7.6	28.1	33.3	29.9	5.1
Octylamine	7.1	13.2	19.4	15.0	25.2	6.1	9.4	13.0	10.5	17.8
Octadecyl amine	5.0	20.1	24.2	21.6	21.3	2.4	6.3	8.4	7.0	11.5



are mainly distributed within the same size range, as shown in Table 1. There is no significant effect of washing on polyvinylpyrrolidone- and SDS-capped nanoparticles. It is apparent that the DLS profiles of most of the nanoparticles capped post-synthesis show significantly larger particle size distribution and  $D_M$  values in comparison to particles capped *in situ*. This could be due to the delay in the capping process, allowing the nanoparticles to agglomerate before capping, which was confirmed by TEM micrographs of uncapped FeCoNiCuPt nanoparticles (Fig. 3), showing increased particle size and agglomeration with time.<sup>34</sup> If capping occurs during washing, the nanoparticles are capped immediately after they detach with an isolating medium, preventing agglomeration and stabilising the surface of nanoparticles right away after being exposed.<sup>34</sup>

### 3.5 DLS analysis of hydrophobic-agent-capped FeCoNiCuPt nanoparticles

The  $D_{10}$ ,  $D_{50}$ ,  $D_{90}$ , and  $D_M$  values in Table 1 represent the number-weighted particle size distribution of FeCoNiCuPt nanoparticles capped with hydrophobic agents as determined by DLS. For FeCoNiCuPt nanoparticles capped with hydrophobic agents, the  $D_M$  values vary from as low as 5.9 nm for post-synthesis octadecene to a maximum of 61 nm for *in situ* oleylamine capping. Nanoparticles capped with oleic acid, oleylamine, and octadecene tend to have a smaller hydrodynamic diameter after washing out the NaCl particles. The distribution of octylamine and hexadecylamine particle sizes is not substantially impacted by washing. In contrast to particles capped post-synthesis, nearly all of the *in situ* hydrophobic-agent-capped particles exhibit a wider particle distribution ( $D_{90}$ – $D_{10}$ ). This indicates that when a hydrophobic agent was added directly to toluene, the inhibition of NaCl particle dissolution resulted in particle size growth and agglomeration,<sup>21,36</sup> which was also established by TEM micrographs of hydrophobic-agent-capped nanoparticles.

The difference between the hydrodynamic radius obtained from DLS and the particle radius determined by TEM can provide insights into the approximate thickness of the capping layer on the surface of the particles. However, it is complicated for particles surrounded by hydrophilic capping agents, as the DLS also adds the size of water molecules surrounding the capping agent because the surface of the hydrophilic agents contains a hydration layer formed by the surrounding water molecules. That is why the actual size of the capping layer, as well as the actual hydrodynamic particle size, may be smaller than the size calculated using DLS.<sup>40,41</sup> This explains why FeCoNiCuPt particles capped with hydrophilic agents have substantially larger diameters than those coated with hydrophobic agents.

### 3.6 Zeta potential of hydrophilic-agent-capped FeCoNiCuPt nanoparticles

Zeta potential (ZP) refers to the electrical potential at the surface of a nanoparticle in relation to its surrounding medium. A higher zeta potential leads to increased repulsion between nearby nanoparticles, thereby preventing agglomeration and enhancing stability. Generally, nanoparticles with a zeta potential magnitude of  $|ZP| \leq 10$  mV are considered highly unstable and prone to agglomeration; those with a  $|ZP|$  of 10–20 mV are unstable or relatively stable, and those with a  $|ZP|$  of 20–30 mV are moderately stable, while particle suspensions with  $|ZP| \geq 30$  mV are



regarded as highly stable.<sup>42,43</sup> Suspended nanoparticles need  $|ZP| \geq 30$  mV to stabilise electrostatically, while  $|ZP| \geq 20$  mV is required for steric stabilisation.<sup>44</sup>

The zeta potential values of all the capped nanoparticles are shown in Table 1, where polyethylenimine-linear capped nanoparticles are highly stable, as they have  $|ZP| \geq 30$  mV in both coating cases, *in situ* and post-synthesis. Pluronic P123 is a copolymer consisting of two hydrophobic polypropylene oxides and one hydrophilic polyethylene oxide block. The polyethylene oxide blocks have an affinity for interacting with water molecules and develop a negative charge, giving rise to a negative zeta potential,<sup>45</sup> as can be seen in Table 1. The presence of polar groups in polyvinylpyrrolidone can lead to a negative zeta potential.<sup>46</sup> Both Pluronic P123 and polyvinylpyrrolidone are non-ionic polymers, and the formation of hydration shells through their interaction with water molecules can also be the result of a negative potential.<sup>40,41</sup> Polyethylenimine-linear is cationic in nature due to the presence of amino groups<sup>47</sup> in this polymer. Nanoparticles capped by polyethylenimine-linear show the highest stability in all the analysed hydrophilic agents, with ZP values of 32 mV and 32.9 mV for capped *in situ* and post-synthesis, respectively. CTAB is also a cationic surfactant,<sup>48</sup> giving moderate stability to nanoparticles ( $ZP \geq 20$  mV). There is no noticeable impact from the timing of the wash on the nanoparticles coated with either of these cationic agents. SDS acts as an anionic surfactant,<sup>49</sup> which does not show greater stability ( $|ZP| \leq 20$  mV) to our nanoparticle suspensions, while citric acid gives moderate stability to suspended nanoparticles ( $20 \leq |ZP| \leq 30$  mV), and has three carboxylate groups functioning as a triprotic acid.<sup>50</sup> These carboxylate groups adhere to the surfaces of nanoparticles, contributing to a net negative charge,<sup>51</sup> as depicted in Table 1.

### 3.7 Zeta potential of hydrophobic-agent-capped FeCoNiCuPt nanoparticles

Nanoparticles suspended in toluene (hydrophobic-agent-capped nanoparticles) typically exhibit a lower zeta potential compared to their water-soluble versions, as depicted in Table 1. This difference arises because water is a polar solvent, while toluene is nonpolar. The polarity of the surrounding environment can influence the surface charge of the capped nanoparticles and provide better electrostatic stability.<sup>52</sup> All capped hydrophobic nanoparticles exhibit a positive zeta potential, which is a result of the positive surface charge of the metal nanoparticles. Electron lone pairs of amines, such as hexadecylamine, oleylamine, octylamine, and octadecylamine, interact with these surface charges, contributing to the positive zeta potential.<sup>53,54</sup> None of the hydrophobic nanoparticles capped *in situ* exhibit good stability, except oleylamine-capped nanoparticles, which have a ZP value of 24.2 mV and are moderately stable. This confirms the TEM analysis that adding a hydrophobic capping agent after washing out the NaCl particles (post-synthesis capping) is a more effective technique. The only hydrophobic capping agent that exhibits high stability ( $ZP = 33.3$  mV) of capped nanoparticles suspended in toluene is oleylamine-capped post-synthesis nanoparticles.

Analysing DLS plots of capped nanoparticles provides insight into the effective thickness of the metal core and capping layer together,<sup>55</sup> which can lead us to the quantitative analysis of surrounding capping thickness<sup>56</sup> and its effect on the stability of nanoparticles. Especially for hydrophilic nanoparticles suspended in



water, water as a suspension medium gives the benefit of a hydration layer, which significantly impacts their stability by providing the electrostatic and steric barrier and increasing the long-term stability of nanoparticles in water suspension.<sup>57</sup> It is observable in Table 1 that most of the hydrophilic-agent-capped nanoparticles have a higher particle size, which leads them to higher values of zeta potential and greater stability.<sup>40,41,57</sup> Larger hydrodynamic diameter particles often have a more stable suspension ( $|ZP| > 20$  mV), while the majority of nanoparticle suspensions with unstable zeta potentials ( $|ZP| < 20$  mV) typically have low hydrodynamic diameters. This is because the hydration layer of nanoparticles in a stable suspension is often thicker, resulting in higher steric stabilisation and less tendency for agglomeration to occur.<sup>40,57</sup> Polyethylenimine-linear-capped nanoparticles were still able to have greater stability with a  $D_M$  value of 33 nm when capped *in situ*, showing no particular effect of washing on their stability. Nanoparticles dispersed in toluene do not have this advantage due to their nonpolar nature and have a reduced electrostatic interaction.<sup>52</sup> According to the Derjaguin–Landau–Verwey–Overbeek theory,<sup>58</sup> hydrophobic particles should have stronger steric repulsion and van der Waals forces in order to compensate for the absence of electrostatic interactions and achieve suspension stability. Greater stability can also result from capping materials that can improve electrostatic interactions with the suspension and other particles. As shown in Table 1 for oleylamine-capped nanoparticles, a larger hydrodynamic diameter could help them gain steric stability. However, according to Table 1, most of the nanoparticles suspended in toluene lack the high hydrodynamic diameter and higher stability. It can also be seen that most of the particles capped post-synthesis have relatively higher stability (*i.e.*, oleylamine, stearic acid, octylamine and octadecylamine). All things considered, the zeta potential analysis of capped FeCoNiCuPt nanoparticles shows that oleylamine and polyethylenimine are efficient capping agents that improve suspension stability and inhibit agglomeration. It can also be claimed that hydrophilic agents are more stable because of the additional hydration impact, and it has been demonstrated once more that in order to achieve good stability, hydrophobic agents had to be added after the isolating medium had been completely washed out.

## 4 Conclusions

In conclusion, the medium-assisted solid-state reaction for the synthesis of HEA nanoparticles looks promising, where ultrafine NaCl particles of less than 10  $\mu\text{m}$  size were used as the isolating medium. The XRD measurements and Rietveld refinement of the resultant FeCoNiCuPt confirm the formation of a single-phase FCC crystal structure with  $Fm\bar{3}m$  (225) space group. EDS results prove the uniform distribution of all constituent elements, with the atomic weight lying well within the range of the prior-defined HEA composition. TEM analysis of uncapped FeCoNiCuPt HEA nanoparticles shows the growing agglomeration of particles with time and an average particle size increment of about 165% in just 10 days, showing the inability of low-temperature ethanol suspension to withstand the thermodynamic need for agglomeration. For this reason, the use of a suitable capping agent has become necessary to achieve the required particle size and good suspension stability.



The effect of thirteen different capping agents on the particle size and stability of FeCoNiCuPt nanoparticle suspensions was analysed using TEM micrographs, DLS analysis, and measurement of their respective zeta potentials. Hydrophilic capping agents were successful in preventing the particle size growth beyond 5 nm, with Pluronic P123-capped nanoparticles having the smallest average particle size and polyethylenimine-linear showing the highest stability of nanoparticle suspension. It can be claimed that nanoparticles capped by hydrophilic agents retain the particles at a smaller average size and give more stability to the suspension because of the additional hydration impact.

Of all the hydrophobic agents, octadecylamine and stearic acid performed the best at retaining small particles, and oleylamine-capped nanoparticles were the most stable, especially those that were capped post-synthesis. However, capping with hydrophobic agents was difficult without a separate washing step due to the hindrance of the dissolution of the NaCl isolating medium. It has been demonstrated that in order to achieve good stability, hydrophobic agents need to go through the post-synthesis capping method.

The zeta potential and hydrodynamic diameter of capped nanoparticles were examined in order to determine the effective thickness of the capping layer and how it affected the stability of the nanoparticle suspension. Polyethylenimine-linear-capped nanoparticles were found to be a great option, with a small average particle size (<5 nm), as well as high stability ( $|ZP| > 30$  mV) in suspension. This synthesis and capping strategy is expected to be applicable to various HEAs with distinct compositions.

## Author contributions

Anurag Sharma developed the original draft of the manuscript, investigated all of the experiments, and performed formal analysis of the results. Andrew L. Hector, the corresponding author, monitored the research, assisted with article review, and provided supervision throughout the experimental design, methodological development, and data analysis. Both authors evaluated and approved the final version of the manuscript.

## Conflicts of interest

There are no conflicts to declare.

## Data availability

The original data of the XRD, EDS, TEM, DLS, and zeta potential analyses are available from the University of Southampton institutional repository. The standard X-ray patterns of individual elements, Fe (PDF code: 9014285), Co (PDF code: 9011619), Ni (PDF Code: 2100640), Cu (PDF Code: 4105681), and Pt (PDF Code: 1011103) can be obtained from the Crystallography Open Database, (COD), <https://www.crystallography.net/cod/index.php>.

Supplementary information: the elemental mapping images of traces of carbon and oxygen, electron image, and TEM image micrographs of capped nanoparticles. See DOI: <https://doi.org/10.1039/d5fd00088b>.

## Acknowledgements

The authors thank the EPSRC for a studentship to AS (EP/W524621/1) and instrumentation funding (EP/K00509X/1, EP/K009877/1 and EP/V007629/1). We also thank Anton Paar for providing access to the DLS instrumentation. AS extends sincere thanks to Regan Doherty, James Thompson, and the Biomedical Imaging Unit at Southampton General Hospital for their support and guidance in conducting the TEM measurements. Special thanks are also due to Dr Daniel Zabek for his valuable suggestions regarding the DLS analysis.

## References

- 1 J.-W. Yeh, S.-K. Chen, S.-J. Lin, J.-Y. Gan, T.-S. Chin, T.-T. Shun, C.-H. Tsau and S.-Y. Chang, *Adv. Eng. Mater.*, 2004, **6**, 299–303.
- 2 C. Meng, X. Wang, Z. Li, C. Wu, L. Chang, R. Liu and W. Pei, *Mater. Adv.*, 2024, **5**, 719–729.
- 3 C. Bazioti, O. M. Løvvik, A. Poulia, P. Carvalho, A. Azar, P. Mikheenko, S. Diplas and A. E. Gunnæs, *J. Alloys Compd.*, 2022, **910**, 164724.
- 4 X. Liu, J. Li, Z. Li, H. Chu, Z. Pan, H. Pan, S. Zhao and D. Li, *Adv. Opt. Mater.*, 2024, **12**, 2302043.
- 5 Y. Liao, Y. Li, R. Zhao, J. Zhang, L. Zhao, L. Ji, Z. Zhang, X. Liu, G. Qin and X. Zhang, *Natl. Sci. Rev.*, 2022, **9**, nwac041.
- 6 C. Cai, Z. Xin, X. Zhang, J. Cui, H. Lv, W. Ren, C. Gao and B. Cai, *Catalysts*, 2022, **12**, 1050.
- 7 S. Pan, H. Shi, Y. Yu, Y. Li, Y. Chen, C. Li, Y. Sun, Z. Yang and F. Luo, *Chem. Commun.*, 2024, **60**, 11778–11781.
- 8 D. Das, Y. Getahun, F. S. Escobar, R. Romero, A. A. El-Gendy and C. Ramana, *J. Phys. Chem. C*, 2022, **126**, 14255–14263.
- 9 N. Hashimoto, K. Mori, S. Matsuzaki, K. Iwama, R. Kitaura, N. Kamiuchi, H. Yoshida and H. Yamashita, *JACS Au*, 2023, **3**(8), 2131.
- 10 S. Shrestha, B. Wang and P. Dutta, *Adv. Colloid Interface Sci.*, 2020, **279**, 102162.
- 11 U. Das, N. K. Daimari, R. Biswas and N. Mazumder, *Discover Appl. Sci.*, 2024, **6**, 320.
- 12 A. Heuer-Jungemann, N. Feliu, I. Bakaimi, M. Hamaly, A. Alkilany, I. Chakraborty, A. Masood, M. F. Casula, A. Kostopoulou, E. Oh, *et al.*, *Chem. Rev.*, 2019, **119**, 4819–4880.
- 13 J. Liu, C. Liang, X. Zhu, Y. Lin, H. Zhang and S. Wu, *Sci. Rep.*, 2016, **6**, 32631.
- 14 G. R. Dey, C. R. McCormick, S. S. Soliman, A. J. Darling and R. E. Schaak, *ACS Nano*, 2023, **17**, 5943–5955.
- 15 C. M. Da Silva, H. Amara, F. Fossard, A. Girard, A. Loiseau and V. Huc, *Nanoscale*, 2022, **14**, 9832–9841.
- 16 J. Sun, A. Leff, Y. Li and T. J. Woehl, *Nanoscale*, 2023, **15**, 10447–10457.
- 17 J. Zhu, Y. Yang, L. Chen, W. Xiao, H. Liu, H. D. Abruña and D. Wang, *Chem. Mater.*, 2018, **30**, 5987–5995.
- 18 X. Zhang, H. Li, J. Yang, Y. Lei, C. Wang, J. Wang, Y. Tang and Z. Mao, *RSC Adv.*, 2021, **11**, 13316–13328.
- 19 J. He, B. Bian, Q. Zheng, J. Du, W. Xia, J. Zhang, A. Yan and J. P. Liu, *Green Chem.*, 2016, **18**, 417–422.

20 S. Dong, Y. Ju, Y. Jiang, C. Meng, R. Liu, C. Wu and W. Pei, *J. Alloys Compd.*, 2022, **909**, 164748.

21 X. Du, Y. Liu, L. Li, W. Chen and Y. Cui, *J. Mater. Res.*, 2014, **29**, 2921–2927.

22 A. Kumar, A. Sharma, M. Sharma, V. Singh, A. Dhaka and R. S. Dhaka, *J. Alloys Compd.*, 2023, **966**, 171506.

23 C. A. Schneider, W. S. Rasband and K. W. Eliceiri, *Nat. Methods*, 2012, **9**, 671–675.

24 B. Cermenek, B. Genorio, T. Winter, S. Wolf, J. Connell, M. Roschger, I. Letofsky-Papst, N. Kienzl, B. Bitschnau and V. Hacker, *Electrocatalysis*, 2020, **11**, 203–214.

25 Y. Gao, D. Li, R. Zhang, Y. Guo, L. Chen, G. Tian, R. Liu and G. Ge, *Spectrochim. Acta, Part B*, 2022, **198**, 106550.

26 J. Zhang and X. Li, *Biomed. J. Sci. Tech. Res.*, 2023, **53**, 5.

27 M. A. Skinner, D. N. Burrows, G. P. Garmire, J. A. Mendenhall, D. H. Lumb, A. D. Holland and P. J. Pool, *EUV, X-Ray, and Gamma-Ray Instrumentation for Astronomy VI*, 1995, pp. 163–178.

28 L. H. Grey, H. Y. Nie and M. C. Biesinger, *Appl. Surf. Sci.*, 2024, **653**, 159319.

29 B. Song, Y. Yang, M. Rabbani, T. T. Yang, K. He, X. Hu, Y. Yuan, P. Ghildiyal, V. P. Dravid and M. R. Zachariah, *ACS Nano*, 2020, **14**, 15131–15143.

30 P. Neoptolemou, N. Goyal, A. J. Cruz-Cabeza, A. A. Kiss, D. J. Milne and T. Vetter, *Powder Technol.*, 2022, **399**, 116827.

31 A. Tsuda and N. V. Konduru, *NanoImpact*, 2016, **2**, 38–44.

32 P. Bélteky, A. Rónavári, D. Zakupszky, E. Boka, N. Igaz, B. Szerencsés, I. Pfeiffer, C. Vágvölgyi, M. Kiricsi and Z. Kónya, *Int. J. Nanomed.*, 2021, **16**, 3021–3040.

33 E. M. Hotze, T. Phenrat and G. V. Lowry, *J. Environ. Qual.*, 2010, **39**, 1909–1924.

34 N. I. Anaraki, A. Sadeghpour, K. Iranshahi, C. Toncelli, U. Cendrowska, F. Stellacci, A. Dommann, P. Wick and A. Neels, *Nano Res.*, 2020, **13**, 2847–2856.

35 B. J. Babalola, O. O. Ayodele and P. A. Olubambi, *Heliyon*, 2023, **9**, e14070.

36 D. Li, N. Poudyal, V. Nandwana, Z. Jin, K. Elkins and J. P. Liu, *J. Appl. Phys.*, 2006, **99**, 08E911.

37 S. K. Filippov, R. Khusnutdinov, A. Murmiliuk, W. Inam, L. Y. Zakharova, H. Zhang and V. V. Khutoryanskiy, *Mater. Horiz.*, 2023, **10**, 5354–5370.

38 R. F. Domingos, M. A. Baalousha, Y. Ju-Nam, M. M. Reid, N. Tufenkji, J. R. Lead, G. G. Leppard and K. J. Wilkinson, *Environ. Sci. Technol.*, 2009, **43**, 7277–7284.

39 V. Filipe, A. Hawe and W. Jiskoot, *Pharm. Res.*, 2010, **27**, 796–810.

40 V. Figueroa, B. Velasco, L. G. Arellano, V. Domínguez-Arca, A. Cambón, A. Pardo, A. Topete, L. C. Rosales-Rivera, J. A. Soltero and S. Barbosa, *J. Mol. Liq.*, 2024, **398**, 124240.

41 E. Firlar, S. Çınar, S. Kashyap, M. Akinc and T. Prozorov, *Sci. Rep.*, 2015, **5**, 9830.

42 C. Jacobs and R. H. Müller, *Pharm. Res.*, 2002, **19**, 189–194.

43 V. R. Patel and Y. Agrawal, *J. Adv. Pharm. Technol. Res.*, 2011, **2**, 81–87.

44 J. D. Clogston and A. K. Patri, in *Characterization of Nanoparticles Intended for Drug Delivery*, Springer, 2011, vol. 697, pp. 63–70.



45 A. Abuelsamen, S. Mahmud, N. H. Mohd Kaus, O. F. Farhat, S. M. Mohammad, F. S. R. Al-Suede and A. M. S. Abdul Majid, *Polym. Adv. Technol.*, 2021, **32**, 2541–2551.

46 M. Sikder, J. Wang, B. A. Poulin, M. M. Tfaily and M. Baalousha, *Environ. Sci.: Nano*, 2020, **7**, 3318–3332.

47 M. M. Mady, W. A. Mohammed, N. M. El-Guendy and A. A. Elsayed, *Int. J. Phys. Sci.*, 2011, **6**, 7328–7334.

48 F. Mindivan, *Mater. Test.*, 2017, **59**, 729–734.

49 M. S. A. M. Bekmukhametova and R. R. Kashapov, *Mental Health Clinician*, 2017, **10**, 164–168.

50 M. A. Dheyab, A. A. Aziz, M. S. Jameel, O. A. Noqta, P. M. Khaniabadi and B. Mehrdel, *Sci. Rep.*, 2020, **10**, 10793.

51 F. Alzoubi, O. A. Noqta, T. AlZoubi, H. AlJabaly, H. Alkhateeb, M. Alqadi and G. Makhadmeh, *Results Eng.*, 2023, **18**, 101206.

52 A. M. Djerdjev and J. K. Beattie, *Phys. Chem. Chem. Phys.*, 2008, **10**, 4843–4852.

53 F. Dumestre, B. Chaudret, C. Amiens, M. Respaud, P. Fejes, P. Renaud and P. Zurcher, *Angew. Chem., Int. Ed.*, 2003, **42**, 5213–5216.

54 K. Quast, *Miner. Eng.*, 2016, **85**, 130–137.

55 A. Muthuvel, M. Jothibas, C. Manoharan and S. J. Jayakumar, *Res. Chem. Intermed.*, 2020, **46**, 2705–2729.

56 A. Asaikkutti, P. S. Bhavan, K. Vimala, M. Karthik and P. Cheruparambath, *J. Trace Elem. Med. Biol.*, 2016, **35**, 7–17.

57 S. Chen, L. Li, C. Zhao and J. Zheng, *Polymer*, 2010, **51**, 5283–5293.

58 B. Derjaguin, N. Churaev, V. Muller, B. Derjaguin, N. Churaev and V. Muller, *Surface Forces*, 1987, pp. 293–310.

